Analysis of chaotic mixing in plugs moving in meandering microchannels

Zhizhao Che (车志钊), Nam-Trung Nguyen (阮南忠),* and Teck Neng Wong (王德能)†
School of Mechanical and Aerospace Engineering, Nanyang Technological University, 50 Nanyang Avenue, Singapore 639798
(Received 21 July 2011; published 12 December 2011)

Droplets moving in meandering microchannels can serve as a passive and robust strategy to produce chaotic mixing of species in droplet-based microfluidics. In this paper, a simplified theoretical model is proposed for plug-shaped droplets moving in meandering microchannels at Stokes flow. With this model to provide the velocity field, particle tracking, which requires a large computation time, is performed directly and easily without interpolation. With this convenience, a broad survey of the parameter space is carried out to investigate chaotic mixing in plugs, including the channel curvature, the Peclet number, the viscosity ratio, and the plug length. The results show that in order to achieve rapid mixing in plugs in meandering microchannels, a large curvature, a small Peclet number, a moderate viscosity ratio, and a moderate plug length are preferred.

DOI: 10.1103/PhysRevE.84.066309 PACS number(s): 47.61.Ne, 47.61.Jd, 47.51.+a, 47.52.+j

I. INTRODUCTION

Rapid mixing is an important task in a number of microfluidic applications, such as chemical reactions [1], particle synthesis [2], protein crystallization [3], and biological applications [4,5]. When the dimension of the fluidic devices shrinks to micrometer scale, rapid mixing is difficult to achieve because of the laminar flow at low Reynolds numbers [6–8]. Without being stirred by turbulence, mixing occurs mainly via molecular diffusion. In addition, mixing in biological applications is even more difficult because of the low diffusivity, of the order of $D \sim 10^{-11}$ m^2/s for large molecules such as proteins. Numerous methods to enhance mixing in microfluidic devices have been reported [6]. The basic idea of these methods is to increase the contact area between liquid filaments. These methods can be categorized into the two groups of passive and active mixers, depending on whether external actuation is required to stir the fluid filaments. The active mixers require external force, such as electroosmosis [9], magnetism [10], acoustics [11], thermocapillarity [12], pulsating flow [13], or mechanical stirring with moving parts. The active methods can effectively enhance mixing process. However, the actuation parts increase the complexity and reduce the robustness of the microdevices. The other group of micromixers, passive mixers, requires no external energy to stir fluid filaments except the force to deliver fluids in the devices. Without moving parts in the devices, these methods are usually robust and reliable. Various passive mixing techniques have been reported such as multilamination [14,15], injection [16], hydrodynamic focusing [17], and droplet mixing [18–22]. Droplet mixing utilizes the internal recirculating vortices in moving droplets to promote mixing.

Chaotic advection enhances mixing by exponentially increasing the interfacial area between two initially segregated fluids [23,24]. It can be generated in a three-dimensional (3D) microchannel by producing transverse flow with patterned grooves on the wall [25]. The transverse flow to generate chaotic advection can also be produced actively using pulsating pressure [26], electro-osmotic force [27,28], magnetic force [29], etc.

Although transverse flow is generated passively in droplets moving in a straight microchannel, chaotic flow is not formed because of the symmetrical pair of vortices in the droplet. The vortices are steady in a frame of reference moving together with the droplet. The species in the droplet is mixed within each vortex, but not between the two vortices. Therefore, the effect of the recirculating vortices on droplet mixing in a straight microchannel is moderate. To produce chaotic advection in droplets, Song *et al.* [30] proposed a simple but effective method by using meandering microchannels. The vortices in droplets become asymmetrical upon the introduction of curvatures and become unsteady upon a change in the direction of the curvature, i.e., upon the use of a meandering microchannel. Being a passive and efficient mixing method, droplets moving in meandering microchannels have extra advantages. The axial dispersion is reduced by confining the species in droplets [21,31], and the reaction time in droplets can be accurately controlled at the millisecond scale [30]. Song *et al.* [32] conducted a series of mixing experiments in droplets moving in meandering microchannels and verified the scaling analysis for the mixing time. However, as they stated, "This scaling argument is too simple to predict the geometry of the microchannels that produces the most rapid mixing, and more theoretical and experimental work toward this goal will be required." Tung *et al.* [33] investigated the droplet mixing in meandering microchannels with square turns and found that the mixing index can increase eight times compared to that in a straight microchannel. They addressed the droplet deformation at the turns, which contributes to the mixing process. Fries and von Rohr [34] investigated the mixing process in slugs and found that the mixing length could be decreased to 12% compared to that in the straight channel design.

Numerical investigations on flow field or mixing in droplets moving in straight [35–37] or meandering microchannels [34,38,39] have been reported. Some simulations were carried out with interface prediction methods to capture interface shapes [33,37–39], while others assumed flat or curved interface shapes [34–36]. Most of the simulations were performed with two-dimensional (2D) models. One main reason for the lack of 3D simulation is that 3D simulation is computation-time-consuming. The prediction of the interface

*mntnguyen@ntu.edu.sg
†mtnwong@ntu.edu.sg

and the analysis of mixing also increase the complexity and the computation time.

The transfer of species in droplets is an advection dominated process as the Peclet number is high due to the low diffusivity of the species, particularly for large molecules in various lab-on-a-chip applications. In this situation, numerical methods to solve the mass transfer equation may fail, because false diffusion may be a problem which overestimates the diffusion effect [40]. The particle tracking method is often used to consider the chaotic mixing of species [37,39,41,42]. However, to evaluate the results of mixing using the particle tracking method, spatial statistics is often used, which extracts some quantitative variables from the locations of the particles. Therefore, a sufficiently large number of tracer particles is required to be distributed into the flow, which results in a very large computation time for the particle tracking method.

As for theoretical models for flow fields in droplets in microchannels, to the best of our knowledge, two types of models are available. The first model simplifies a parabolic velocity profile in the droplets [19]. Therefore, the model is valid only when the droplet is sufficiently long, because the transverse flow at the front and the rear of the droplet is not considered. The other type of model is for droplets with spherical shapes surrounded by another fluid [43–45]. The confinement by the channel wall is not considered. Therefore, this model is not practical for mixing in plugs. Here, *plugs* refer to the droplets that occupy the entire width of the microchannels.

In this paper, we present a simplified 2D theoretical model for plug trains in meandering microchannels. Here, we use a *plug train* to represent a series of N consecutive different plugs which repeat periodically in microchannels, as shown in Fig. 1(d). This model is then used to analyze chaotic mixing in plugs. The chaotic mixing process is investigated using the particle tracking method. The proposed model shows two advantages over the numerical methods for particle tracking analysis. First, the computation time for obtaining the flow field is significantly reduced. Therefore, the particle tracking simulation, which requires a large amount of tracer particles and a long computation time, can be performed more easily with the flow field from the model. Second, the model can provide velocities in the whole flow domain, while numerical methods can only provide information at a set of discrete points. Hence, particle tracking simulation can be performed directly on the flow field from the model, and interpolation error is avoided. We believe that our model complements the numerical work by providing a simple and efficient way to analyze chaotic mixing in plugs with a broad survey of the parameter space.

In a 3D curved channel, Dean vortices may be generated due to the imbalance between the centrifugal force and the radial pressure difference [46]. The vortices get stronger when the Dean number increases, which characterizes the relative effect of the centrifugal force with the viscous force, $\mathrm{De} \equiv \frac{\rho V D_H}{\mu}\sqrt{\frac{D_H}{2R}} = \mathrm{Re}\sqrt{\frac{D_H}{2R}}$, where ρ and μ are, respectively, the density and the dynamic viscosity of the fluid, V is the axial velocity, D_H is the hydraulic diameter of the channel, R is the radius of the curved channel path, and $\mathrm{Re} = \frac{\rho V D_H}{\mu}$ is the Reynolds number. However, due to the small dimension and the low flow speed in microchannels, the Reynolds number Re and the Dean number De are usually much less than 1. The centrifugal force is usually very small, and this effect is negligible in most microfluidic devices. Therefore, the Dean vortices are much weaker than those in channels of large scale. The 2D model presented in this paper does not consider Dean vortices, which are insignificant in most microfluidics devices, but considers the vortices generated due to the presence of the interface, which are strong even in flows with low Reynolds numbers.

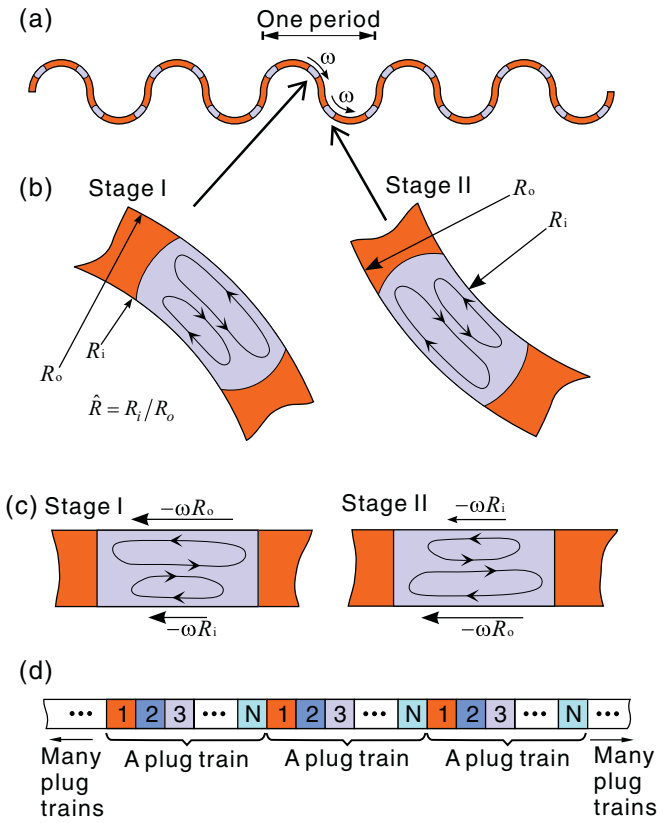

FIG. 1. (Color online) Schematic diagram of plugs moving in a meandering microchannel. (a) Plugs moving in a meandering microchannel. (b) Flow patterns in plugs at different stages of the meandering microchannel. Vortices of different sizes are formed near the wall of the microchannel. The vortex near the inner wall (with radius R_i) is smaller, while the vortex near the outer wall (with radius R_o) is larger. (c) Simplified rectangular-shaped plugs with sliding walls in a frame of reference moving with the plugs. In stage I, as shown on the left, the sliding velocities on the top and bottom walls are, respectively, $-\omega R_i$ and $-\omega R_o$. When the plug arrives at a location with a different curvature (stage II), the sliding velocities on the top and bottom walls exchange. (d) A *plug train* refers to a series of N consecutive different plugs which repeat periodically.

The paper is organized as follows. In Sec. II, the theoretical model is presented and then validated against experimental results. The particle tracking method for analyzing and evaluating the mixing process is presented in Sec. III. In Sec. IV, the mechanism to enhance mixing is elaborated, and the parameters, such as the curvature of the microchannel, the Peclet number, the length of the plug, and the viscosities of the fluids, are investigated.

II. MATHEMATICAL MODELING OF THE FLOW FIELD

A. Problem description

Figure 1(a) illustrates plug flow in a 2D meandering microchannel with two immiscible phases. A *period* of meandering microchannel refers to a section of channel with two semicircles. The curvature of the microchannel is represented by the radius ratio of the inner wall and outer wall $\hat{R} \equiv R_i/R_o$, where R_i and R_o are, respectively, the radii of the inner wall and outer wall toward the center of the channel path. A smaller value of $\hat{R}$ indicates a larger curvature, and vice versa, as shown in Fig. 1(b). When a plug is moving in a microchannel, a pair of vortices is formed in the plug due to the presence of the interfaces [19]. In a frame of reference moving together with the plug, the plug experiences different sliding velocities on each wall, which are proportional to the radius toward the center of the channel path [47]. The inner wall has a lower sliding velocity ωR_i, while the outer wall has a higher sliding velocity ωR_o, where ω is the angular speed of the plug with the center point of the channel path. Therefore, the vortex near the inner wall is smaller, while the one near the outer wall is larger.

As the plug moves at different stages of the meandering microchannel, the vortex pattern varies with the change of the channel curvature. When the plug is moving in the first semicircle (stage I), the vortex near the top wall is larger, while the vortex near the bottom wall is smaller. As the plug moves into the second semicircle (stage II), the two vortices exchange in size, as shown in Fig. 1(b). The plugs at different stages of the meandering microchannel can be simplified to rectangular shapes, and the sliding velocities due to the channel curvature are applied on the top and bottom walls of the rectangular plugs, as shown in Fig. 1(c). This method to simplify the flow was used by Sivasamy *et al.* [48] and by Blanchette [43]. The sliding velocities of the top and bottom walls are denoted $-S_1(t)$ and $-S_2(t)$, respectively. At stage I, $S_1 = \omega R_o$ and $S_2 = \omega R_i$, while at stage II, $S_1 = \omega R_i$ and $S_2 = \omega R_o$. The speed of the plugs is $V = [S_1(t) + S_2(t)]/2$, which remains constant over time.

Figure 1(a) shows schematic diagrams of plugs with two immiscible phases. A more general case is a series of consecutive plugs with N different properties, such as different lengths, viscosities, densities, or chemical contents. Any two consecutive plugs are immiscible to each other. Here, we use *plug train* to refer to a series of N consecutive different plugs which repeat periodically in microchannels, as shown in Fig. 1(d).

B. Mathematical modeling of the flow in plug trains

To model the flow field mathematically, a Cartesian coordinate system (CS) is built on each of the N plugs, as shown in Fig. 2. For plug i ($1 \leqslant i \leqslant N$), the coordinate system CS-i (x_i, y_i) is built with the origin O_i at the center of plug i. Therefore, plug i takes the region of $-L_i \leqslant x_i \leqslant L_i$, $-h \leqslant y_i \leqslant h$, $2h$ denotes the width of the microchannel, and $2L_i$ denotes the length of plug i. All CSs, CS-i ($i = 1 \ldots N$), are translating toward right at the speed of V. Consequently, the N plug units

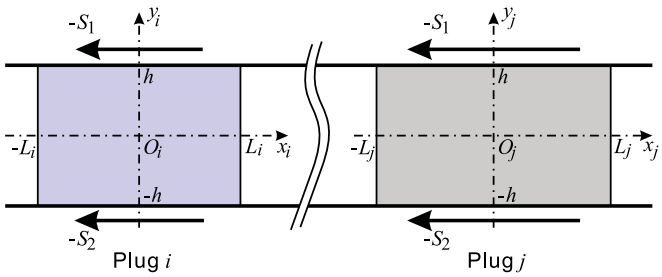

FIG. 2. (Color online) Cartesian coordinate systems for a plug train moving in a microchannel.

are stationary with respect to their own translating CSs. The transformation between any two CSs (CS-i and CS-j) is

$$x_j = x_i + L_i + L_j + 2\sum_{k=i+1}^{j-1} L_k, \tag{1}$$

$$y_i = y_j, \tag{2}$$

where $0 \leqslant i < j \leqslant N$.

Due to the small dimension of the microchannel, the gravitational force is negligible. The fluid is assumed to be incompressible Newtonian fluid. Due to the low Reynolds number, the flow can be simplified to the Stokes flow. The governing equation for plug i is biharmonic [49–51]:

$$\left(\frac{\partial^4}{\partial {x_i}^4} + 2\frac{\partial^4}{\partial {x_i}^2 \partial {y_i}^2} + \frac{\partial^4}{\partial {y_i}^4}\right)\varphi_i = 0, \tag{3}$$

where φ_i is the stream function in plug i ($1 \leqslant i \leqslant N$) which satisfies

$$u_{x,i} = \frac{\partial \varphi_i}{\partial y_i}, \quad u_{y,i} = -\frac{\partial \varphi_i}{\partial x_i}. \tag{4}$$

By incorporating the boundary conditions, Eq. (3) can be solved and the series solution of the velocity field can be obtained in a dimensionless form as follows:

$$\hat{u}_{x,i} = \sum_{m=1}^{\infty}\left[{p_m^o}'(\hat{y}_i) + {p_m^e}'(\hat{y}_i)\right]\frac{(-1)^m}{\alpha_m}X_m\cos(\alpha_m\hat{x}_i) + \hat{L}_i\sum_{l=1}^{\infty}(-1)^l\left[q_l^e(\hat{x}_i)\,Y_l^e + q_l^o(\hat{x}_i)\,Y_l^o\right]\cos(\beta_l\hat{y}_i), \tag{5}$$

$$\hat{u}_{y,i} = \sum_{m=1}^{\infty}\left[p_m^o(\hat{y}_i)\,X_m^o + p_m^e(\hat{y}_i)\,X_m^e\right](-1)^m\sin(\alpha_m\hat{x}_i) - \hat{L}_i\sum_{l=1}^{\infty}\frac{(-1)^l}{\beta_l}\left[q_l^{e\prime}(\hat{x}_i)\,Y_l^e + q_l^{o\prime}(\hat{x}_i)\,Y_l^o\right]\sin(\beta_l\hat{y}_i). \tag{6}$$

The details for obtaining the solution are provided in Appendix A.

To examine the 2D assumption, and to study the 3D effect on the flow pattern within liquid plugs, numerical simulations of a plug unit were carried out, and the results are provided in Appendix B.

C. Comparison with experimental results

To validate the 2D model, comparison has been made with the experimental velocity field reported by Günther *et al.* [52], as shown in Fig. 3. The fluids used in the experiment are air and ethanol. The viscosities are, respectively, $\mu_{\text{air}} = 1.827 \times 10^{-5}$ Pa · s and $\mu_{\text{ethanol}} = 1.07 \times 10^{-3}$ Pa · s. The velocity field in the ethanol plug was measured using micro particle image velocimetry (μPIV). The dimensionless plug length $\hat{L} = 1.57$ is estimated in pixels from Fig. 3(b) as $\hat{L} \equiv \frac{L_{\text{pixel}}}{w_{\text{pixel}}} = \frac{A_{\text{pixel}}}{w_{\text{pixel}}^2}$, where L_{pixel}, w_{pixel}, and A_{pixel} are the length of the ethanol plug, the width of the microchannel, and the area of the ethanol plug in pixels, respectively. The agreement with the experimental results indicates that the 2D model is capable of capturing the main flow features in the plug. The streamline in the plug is shown in Fig. 3(g). The pair of vortices can be clearly observed. The upper vortex **A** is circulating in the anticlockwise direction with positive stream function $\hat{\varphi}_A$; the lower vortex **B**, in the clockwise direction with negative stream function $\hat{\varphi}_B$. A streamline S-S separates these two vortices with $\hat{\varphi}_{\text{S-S}} = 0$.

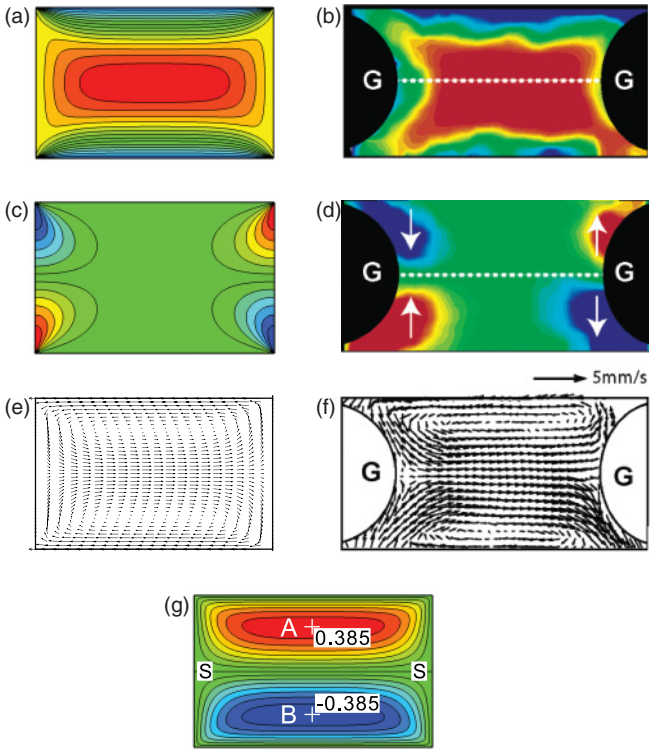

FIG. 3. (Color online) Flow field in an ethanol plug of an ethanol/air plug train moving in a microchannel with $\hat{L}$ =1.57: (a) $\hat{u}_x$ from the 2D model. (b) u_x from μPIV [52]. (Reprinted with permission from [52]. Copyright 2005 American Chemical Society.) (c) $\hat{u}_y$ from the 2D model. (d) u_y from μPIV [52]. (Reprinted with permission from [52]. Copyright 2005 American Chemical Society.) (e) Dimensionless velocity vectors from the 2D model. (f) Velocity vectors from μPIV [52]. (Reprinted with permission from [52]. Copyright 2005 American Chemical Society.) (g) Contours of dimensionless stream function $\hat{\varphi}$ from the 2D model with the increment between two successive streamlines $\Delta\hat{\varphi} = 0.05$. The crosses and the corresponding values are the locations and the magnitudes of the maximum/minimum of the dimensionless stream function.

III. SIMULATION OF MIXING BY THE PARTICLE TRACKING METHOD

A. Convection-diffusion equation

The convection-diffusion equation that governs the transfer of species in the plug is

$$\frac{\partial C}{\partial t} + u_x \frac{\partial C}{\partial x} + u_y \frac{\partial C}{\partial y} = D\left(\frac{\partial^2 C}{\partial x^2} + \frac{\partial^2 C}{\partial y^2}\right). \tag{7}$$

The above equation can be nondimensionalized by introducing the following dimensionless group:

$$\begin{aligned} &\hat{x} \equiv x/h, \quad \hat{y} \equiv y/h, \quad \hat{t} \equiv tV/h, \\ &\hat{u}_x \equiv u_x/V, \quad \hat{u}_y \equiv u_y/V, \quad \text{Pe} \equiv \frac{hV}{D}, \end{aligned} \tag{8}$$

where Pe is the Peclet number. We can obtain that

$$\frac{\partial C}{\partial \hat{t}} + \hat{u}_x \frac{\partial C}{\partial \hat{x}} + \hat{u}_y \frac{\partial C}{\partial \hat{y}} = \frac{1}{\text{Pe}}\left(\frac{\partial^2 C}{\partial \hat{x}^2} + \frac{\partial^2 C}{\partial \hat{y}^2}\right). \tag{9}$$

Therefore, particle tracking simulation is performed in a dimensionless scale and the Peclet number is used to consider the relative effect between convection and diffusion.

B. Advection by the flow

Evaluation of the performance of the mixing process uses the particle tracking method, which places passive, noninteracting particles in the flow fields to observe the advection and diffusion of these particles and to visualize the mixing effect. The tracer particles are advected by the flow in dimensionless form as follows:

$$\frac{d\hat{x}(\hat{t})}{d\hat{t}} = \hat{u}_x(\hat{t}), \quad \frac{d\hat{y}(\hat{t})}{d\hat{t}} = \hat{u}_y(\hat{t}). \tag{10}$$

The above equations were integrated using the fourth-order Runge-Kutte method. Different time steps were repeatedly refined until passive particles faithfully followed the streamline in the plug. The dimensionless time step used in the simulation was $\Delta\hat{t} = 10^{-3}$.

Integrating Eq. (10) requires information on velocity at any spatial location ($-\hat{L} \leqslant \hat{x} \leqslant \hat{L}$, $-1 \leqslant \hat{y} \leqslant 1$). The series expression of the flow field in Eqs. (5) and (6) shows an advantage of the particle tracking simulation because it offers the solution at any point in the domain, rather than the solution at a set of discrete grid points.

C. Diffusion by random walk

The diffusion of the passive particles is simulated using the random walk method [37],

$$x_k = x_k^* + \zeta_{x,k}\sqrt{2D\Delta t}, \quad y_k = y_k^* + \zeta_{y,k}\sqrt{2D\Delta t}, \tag{11}$$

where (x_k^*, y_k^*) is the location of particle k after the advection time step, D is the diffusivity of the species in the liquid plug, and $\zeta_{x,k}$ and $\zeta_{y,k}$ are two independent random numbers with

normal distribution for particle k at the current time step. After nondimensionalization, Eq. (11) becomes

$$\hat{x}_k = \hat{x}_k^* + \zeta_{x,k}\sqrt{\frac{2\Delta\hat{t}}{\mathrm{Pe}}}, \quad \hat{y}_k = \hat{y}_k^* + \zeta_{y,k}\sqrt{\frac{2\Delta\hat{t}}{\mathrm{Pe}}}. \tag{12}$$

The tracer particle may go out of the plug domain due to the random walk by diffusion or integration error by advection. The particles crossing the boundary are mirror-reflected back to the plug [37].

D. Evaluation of mixing

The mixing process is characterized and evaluated by the mixing index, η [53]. To calculate the mixing index at an instant t, the plug domain is divided into M equal-size bins. The standard deviation of particle numbers in the bins is then calculated as follows:

$$\sigma(t) = \sqrt{\frac{1}{M}\sum_{j=1}^{M}(c_j(t) - \bar{c})^2}, \tag{13}$$

where M is the number of bins ($M = 40 \times 20$ in the simulation), $c_j(t)$ is the number of particles in bin j at time t, and $\bar{c}$ is the average number of particles per bin in the ideal-mixed case,

$$\bar{c} = \frac{N_P}{M}, \tag{14}$$

where N_P is the total number of particles used for particle tracking ($N_P = 20\,000$ in the simulation). During the mixing process, the standard deviation σ_0 is initially large, then decreases gradually. Ideally, $\sigma(t)$ finally approaches 0 when the fluid particles are homogeneously dispersed in the whole domain. In simulation, when the particles achieve complete spatial randomness, $\sigma(t)$ approaches an asymptotic limit depending on N_P and M [54]. The mixing index η is the standard deviation normalized by the initial standard deviation σ_0, which is the most segregated case:

$$\eta = \frac{\sigma(t)}{\sigma_0}. \tag{15}$$

In addition, when the tracer particles achieve the complete spatial randomness, the asymptotic limit of the mixing index is $\eta_{\mathrm{asymp}} = 1/\sqrt{N_P}$ [54]. In this investigation, $N_P = 20\,000$, therefore, $\eta = 0.00707$ indicates the homogeneous state with randomly distributed particles. As the mixing progresses, η varies from unity to 0.00707.

E. Particle tracking algorithm

The algorithm for the particle tracking method with the random walk method is summarized as follows:

(1) Initialize the locations of the particles, i.e., $(\hat{x}_k, \hat{y}_k)$.

(2) Determine the velocity of each particle from Eqs. (5) and (6), i.e., $(\hat{u}_{x,k}, \hat{u}_{y,k})$.

(3) Integrate Eq. (10) to get the location of the particle after advection, i.e., $(\hat{x}_k^*, \hat{y}_k^*)$.

(4) Determine the location of the particle after random walk using Eq. (12), i.e., $(\hat{x}_k, \hat{y}_k)$.

(5) Check whether any particle goes out of the plug. For a particle out of the plug, reflect it back to the plug with mirror reflection.

(6) Calculate the mixing index η using Eq. (15).

Steps 2–6 are repeated until the plug goes out of the microchannel.

IV. RESULTS AND DISCUSSION

A. The mechanism of plug mixing in a meandering microchannel

In the following analysis, the results are limited to mixing within the first plug of a plug train with two plugs, i.e., $N = 2$. For plug trains with more plugs ($N > 2$), simulation can be carried out similarly by replacing the flow field with that in the corresponding plug.

When a liquid plug moves in a meandering microchannel, three effects on the mixing—stretching, folding, and diffusion—interplay as the mixing progresses. They are illustrated in Fig. 4 and explained as follows.

1. Stretching of liquid filaments by the vortices

The effect of stretching of liquid filaments by the vortices is shown in Fig. 4(a). Initially, all the tracer particles are evenly placed in a statistical bin ($0.3 < x < 0.4$, $0.3 < y < 0.4$). Blue and red color is used to distinguish the particles in the upper and lower halves of the rectangular bin. As the liquid

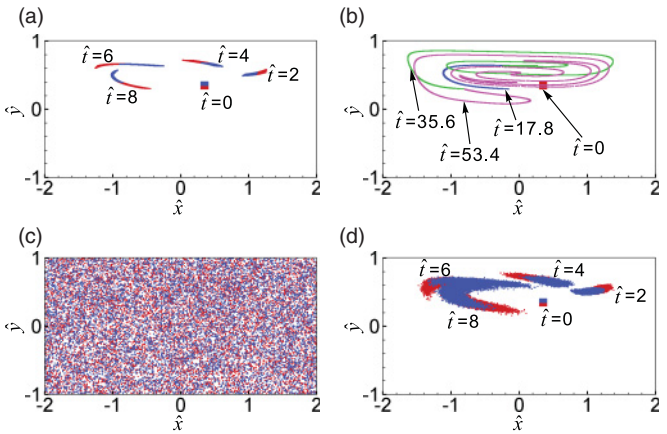

FIG. 4. (Color online) Mechanisms to enhance mixing in a plug moving in meandering microchannels: stretching of liquid filaments by vortices, folding of liquid filaments by changing channel curvature, and diffusion. The dimensionless plug length is $\hat{L} = 2$, the radius ratio of the microchannel is $\hat{R} = 0.7$, and the viscosity ratio is $\mu_1/\mu_2 = 1$. (a) Stretching of liquid filaments in a liquid plug as it is moving in a microchannel. (b) Folding of liquid filaments by alternation of the direction of the channel curvature. The scattering of tracing particles at different times ($\hat{t} = 0$, 17.8, 35.6, 53.4) illustrates the folding effect. The corresponding locations of the plug in the meandering microchannel are, respectively, 0, 0.5, 1, 1.5, and 2 periods. (c) Poincaré section for a plug flowing in a meandering microchannel (for 1000 periods with 20 particles). This Poincaré section was generated by releasing tracer particles into the flow and recording their positions after each period of the meandering microchannel. (d) Scattering of tracer particles by the diffusion effect, which accelerates the mixing process. The Peclet number $\mathrm{Pe} = 10^4$.

plug is moving forward, the particle blob is stretched by the recirculating flow, as shown in Fig. 4(a), from $\hat{t} = 0$ to $\hat{t} = 8$. The stretching increases the contact area of the tracer particles with the surrounding fluid. A velocity gradient is necessary to stretch the liquid filaments. During advection, a larger velocity gradient is preferred because it results in two adjacent tracer particles departing rapidly from each other.

2. *Folding of fluid filaments by changing channel curvature*

The flow within the plug is dominated by a pair of counter-rotating vortices. In a straight channel, the tracer particles faithfully follow the streamlines of their own vortex, and diffusion is the only mechanism that can transfer the tracer particles across different vortices. In contrast, for a meandering microchannel, once the direction of the channel curvature changes, the sizes of the two vortices exchange. Consequently, some tracer particles that originally follow one vortex may follow the other vortex. Therefore, the exchange of the vortex pattern can greatly enhance the transfer of particles across vortices by flow advection and, thereafter, facilitate the mixing process in the liquid plug. The folding effect, together with the stretching effect, produces entangled long liquid filaments in the plug, as shown in Fig. 4(b).

Poincaré section is a tool to reveal the chaotic nature of mixers [23,24]. To study the combination of stretching and folding of liquid filaments, a Poincaré section for plug flow in a meandering microchannel with $\hat{R} = 0.7$ was constructed as shown in Fig. 4(c). This Poincaré section was generated by releasing 20 tracer particles into the flow and recording their positions after each period of the meandering microchannel. The flow can advect the particles throughout the plug. Therefore, the meandering microchannel can result in chaotic behavior of the particles upon exchange of the sizes of the two vortices in plugs.

3. *Diffusion*

The effect of diffusion on mixing is shown in Fig. 4(d). Diffusion has the effect of reducing the concentration gradient. The combining effect of stretching and folding can effectively create entangled liquid filaments, as shown in Fig. 4(b). Diffusion, at the same time, blurs the interface of the liquid filaments with the surrounding fluid.

4. *A typical result*

With the effects of stretching, folding, and diffusion, the mixing process in a typical liquid plug is shown in Fig. 5. Initially, all the tracer particles ($N_P = 20\,000$) are evenly placed in a bin ($0.3 < x < 0.4$, $0.3 < y < 0.4$). The particles are advected by the vortices and stretched into a long thin filament. When the plug enters the next stage, the fluid filament of tracer particles follows the new streamlines. Therefore, exchange of the vortex pattern entangles the fluid filament of tracer particles. At the same time, diffusion can effectively blur the interface between the tracer particles and the surrounding fluid. In this way, as the time passes as shown in Fig. 5, a group of tracer particles initially located in a bin ($\hat{t} = 0$) first expands to take the top half of the plug ($\hat{t} = 50$), gradually transfers to the bottom half of the plug ($\hat{t} = 100$), then disperses throughout the plug ($\hat{t} = 200$), and, finally, achieves a homogeneous state with randomly distributed particles.

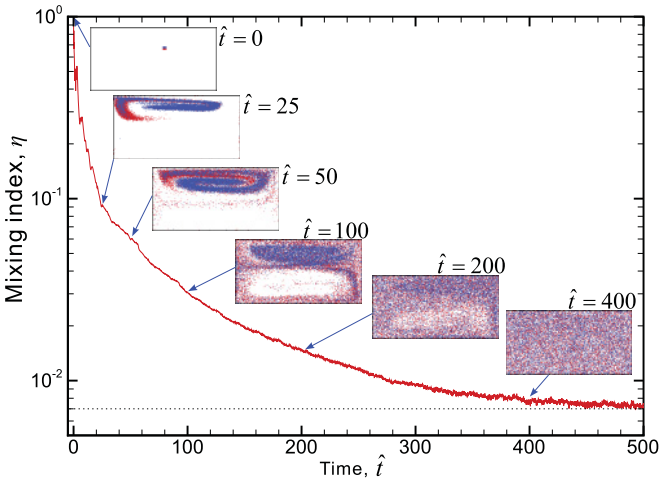

FIG. 5. (Color online) Mixing process in a typical liquid plug under the effects of stretching, folding, and diffusion. The dashed horizontal line $\eta_{\text{asymp}} = 0.00707$ indicates the homogeneous state with randomly distributed particles. The radius ratio of the microchannel is $\hat{R} = 0.7$, the Peclet number is $\text{Pe} = 10^4$, the viscosity ratio is $\mu_1/\mu_2 = 1$, and the dimensionless plug length is $\hat{L} = 2$.

B. Effect of curvature

The effect of curvature on the mixing process in plugs is shown in Fig. 6. Variation of the mixing indices with time is plotted in Fig. 6(a), and the corresponding flow patterns and mixing pattern are shown in Figs. 6(b) and 6(c), respectively. In a straight microchannel, the two counter-rotating vortices in a plug are of equal size. If the microchannel is curved, the two vortices become asymmetric. The size difference between the two vortices increases with an increase in the curvature, as shown in Fig. 6(b). Therefore, with a larger curvature (such as $\hat{R} = 0.5$), the folding effect is applied to more liquid filaments at the location where the curvature direction changes. Consequently, a larger curvature produces rapid mixing in the plug, while a smaller curvature (such as $\hat{R} = 0.9$) results in slow mixing, as shown in Fig. 6(a). The corresponding mixing patterns at the instant $\hat{t} = 100$ are shown in Fig. 6(c). With a large curvature ($\hat{R} = 0.5$), a homogeneous state of randomly distributed particles is almost achieved at $\hat{t} = 100$. In contrast, the tracer particles only occupy the top half of the plug at a small curvature ($\hat{R} = 0.9$). These results show that a larger curvature is preferred for rapid plug mixing in meandering microchannels.

C. Effect of Peclet number

The effect of the Peclet number on the mixing process is shown in Fig. 7. At a high Peclet number, the mixing process is dominated by advection. As the Peclet number decreases, the relative effect of diffusion increases. Diffusion can effectively smear the interface between liquid filaments of different species. The diffusion effect decreases with increasing Pe. Therefore, at a high Peclet number, such as $\text{Pe} = \infty$, mixing is slow. In addition, the mixing index fluctuates when a large

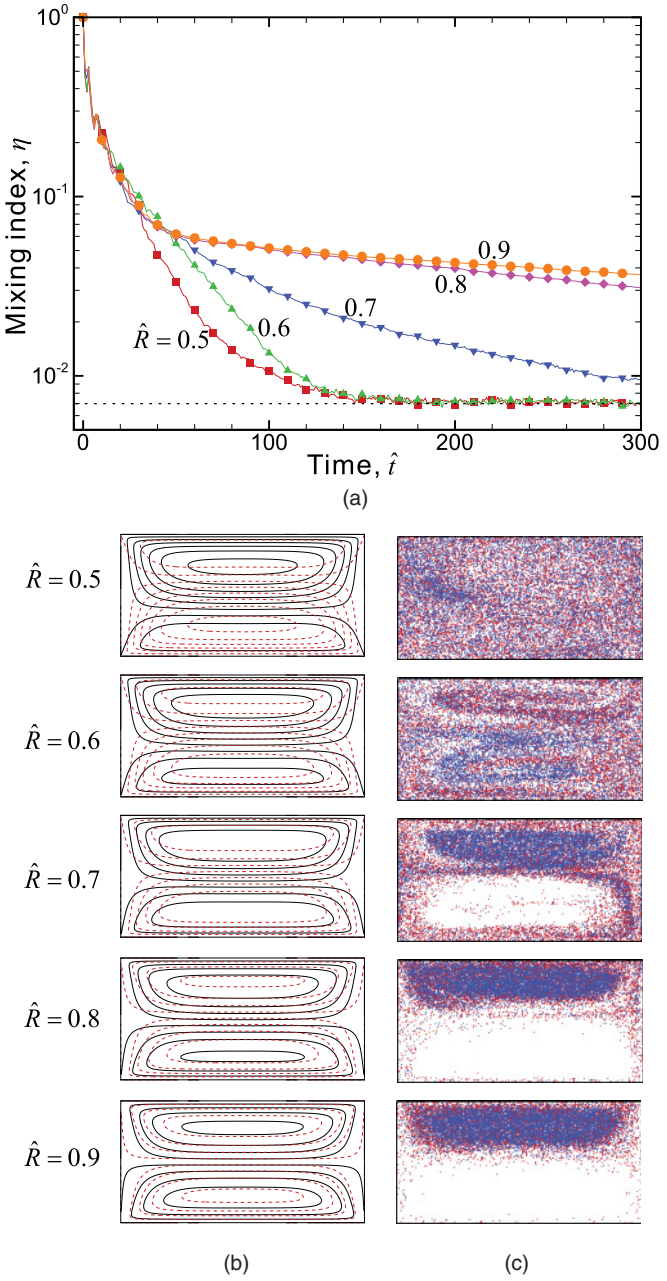

FIG. 6. (Color online) Effect of curvature on the mixing process in plugs. The Peclet number is Pe $= 10^4$, the viscosity ratio is $\mu_1/\mu_2 = 1$, and the dimensionless plug length is $\hat{L} = 2$. (a) Variation of mixing indices with time for microchannels of different curvatures. The dashed horizontal line $\eta_{\text{asymp}} = 0.00707$ indicates the homogeneous state with randomly distributed particles. (b) Flow pattern in plugs moving in meandering microchannels with different curvatures. Solid (black) contours indicate streamlines at stage I, while dashed (red) contours indicate streamlines at stage II. (c) Visualization of mixing patterns at $\hat{t} = 100$ for microchannels with different curvatures.

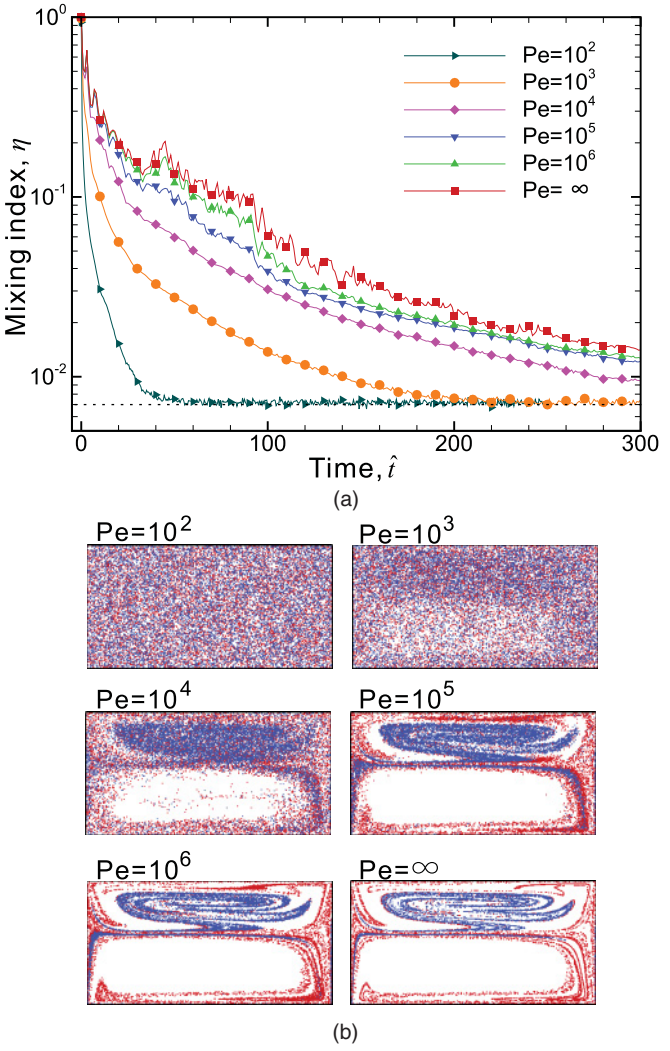

FIG. 7. (Color online) Effect of the Peclet number on mixing process in plugs. The radius ratio of the meandering microchannel is $\hat{R} = 0.7$, the viscosity ratio is $\mu_1/\mu_2 = 1$, and the dimensionless plug length is $\hat{L} = 2$. (a) Variation of mixing indices with time for different Peclet numbers. The dashed horizontal line $\eta_{\text{asymp}} = 0.00707$ indicates the homogeneous state with randomly distributed particles. (b) Visualization of mixing patterns at $\hat{t} = 100$ for different Peclet numbers.

amount of tracer particles moves together from one statistical bin to another. At a low Peclet number, such as Pe $= 10^2$, mixing is rapid due to the strong effect of diffusion. Because diffusion can smear the interface between the region of tracer particles and the surrounding area, the fluctuation of mixing index is insignificant, as shown in Fig. 7(a). To show the variation of the mixing indices with the change in the Peclet number, we plot the particle distributions at $\hat{t} = 100$ and compare them in Fig. 7(b). At a low Peclet number (Pe $= 10^2$), a homogeneous state of randomly distributed particles is achieved at $\hat{t} = 100$. In contrast, at a high Peclet number (Pe $= \infty$), tracer particles are stretched into thin filaments and are mainly distributed in the top half of the plug. Therefore, a low Peclet number is preferred for rapid plug mixing in meandering microchannels.

D. Effect of viscosity

As shown in Fig. 8, the effect of the viscosity ratio μ_1/μ_2 on the mixing process is not as significant as that of the channel curvature or the Peclet number. The mixing indices are plotted against time for different viscosity ratios in Fig. 8(a).

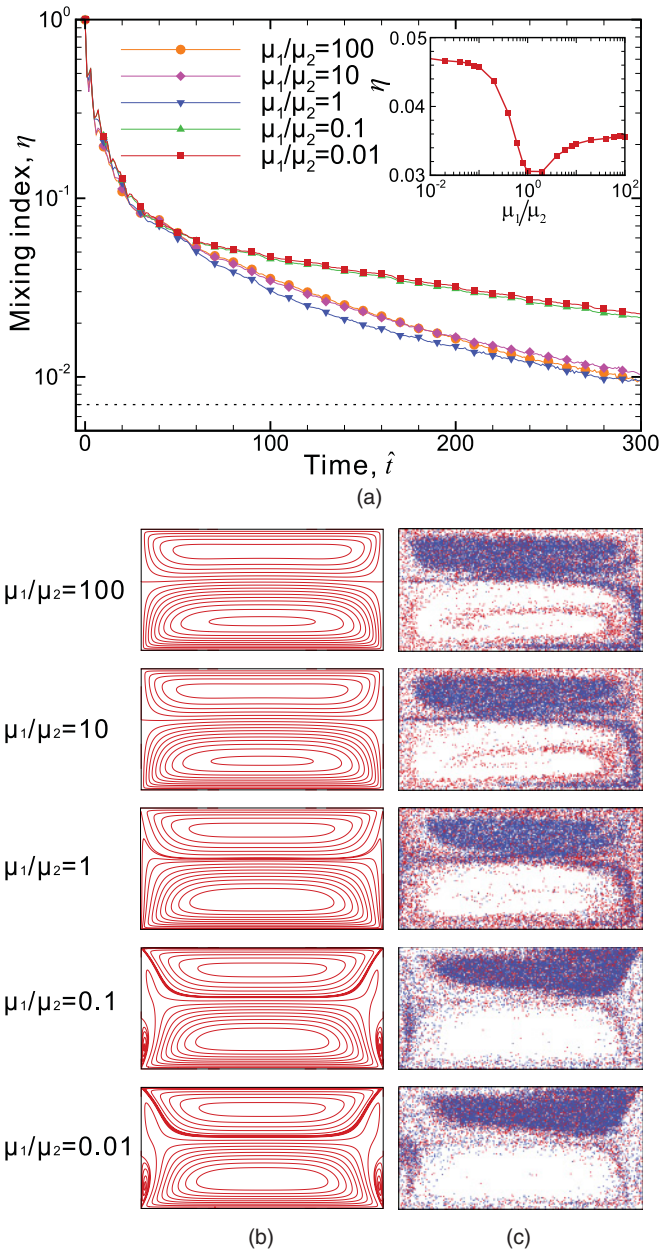

FIG. 8. (Color online) Effect of the viscosity ratio on the mixing process in plugs. The radius ratio of the meandering microchannel is $\hat{R} = 0.7$, the Peclet number is $\mathrm{Pe} = 10^4$, and the dimensionless plug length is $\hat{L} = 2$. (a) Variation of mixing indices with time in plugs of different viscosities. The dashed horizontal line $\eta_{\mathrm{asymp}} = 0.00707$ indicates the homogeneous state with randomly distributed particles. Inset: Variation of mixing indices with viscosity ratio at $\hat{t} = 100$. (b) Flow pattern in plugs for fluids of different viscosities; secondary vortices are formed when the viscosity ratio μ_1/μ_2 is low. (c) Visualization of mixing patterns at $\hat{t} = 100$ for fluids of different viscosities.

To show the variation of the mixing indices as the viscosity ratio changes, the mixing indices were probed and compared at $\hat{t} = 100$ in the inset in Fig. 8(a). The flow streamlines in plugs are plotted in Fig. 8(b), and the distribution of tracer particles at $\hat{t} = 100$ is shown in Fig. 8(c). At a high viscosity ratio ($\mu_1/\mu_2 = 100$), the mixing index at $\hat{t} = 100$ is

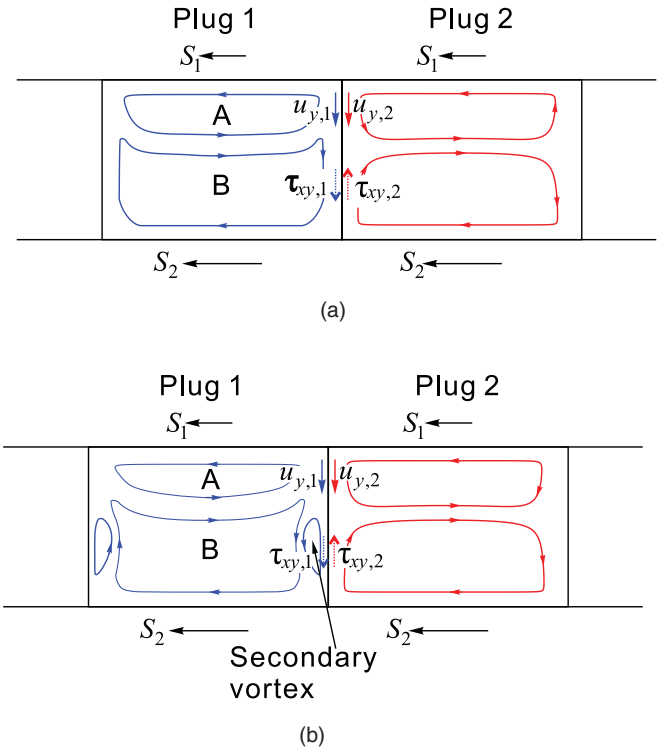

FIG. 9. (Color online) Flow diagrams of plug trains with different viscosity ratios: (a) distortion of vortex pattern by shear stress at the interface $\tau_{xy,2}$; (b) formation of secondary vortices when the shear stress is sufficiently high due to the low viscosity ratio μ_1/μ_2.

$\eta_{\hat{t}=100} = 0.0355$. If the viscosity ratio decreases, the mixing index also decreases, such as $\mu_1/\mu_2 = 1$, which indicates rapid mixing in the plug. If the viscosity ratio decreases further, such as $\mu_1/\mu_2 = 0.01$, the mixing index increases, which indicates relatively slow mixing in the plug.

The variation of mixing performance with the viscosity ratio can be explained from the vortex pattern in the plug. At the interface between the two plugs, the tangential stress acting on the left side of the interface is $\tau_{xy,1}$, while the tangential stress acting on the right side of the interface is $\tau_{xy,2}$. The two shear stresses should be balanced, as shown in Fig. 9. At a high viscosity ratio (such as $\mu_1/\mu_2 = 100$), the vortex pattern is shown in Fig. 8(b). The effect of shear stress on the flow in plug 1 is insignificant because plug 1 is extremely viscous and the flow inside is difficult to be deformed. If the viscosity ratio decreases, the viscosity in plug 1 decreases, and the effect of shear stress on the flow in plug 1 increases. Because the vortex near the inner wall (vortex **A**) is relatively smaller and weaker than the vortex near the outer wall (vortex **B**), vortex **A** is first affected when the viscosity ratio is decreasing. The fluid in plug 1 near the interface is dragged downward by the shear stress $\tau_{xy,2}$, which is in the opposite direction from vortex **A** and in the same direction as vortex **B**. Therefore, vortex **A** shrinks while vortex **B** expands and occupies the region near the interface, as illustrated in Fig. 9(a). The distorted vortex pattern increases the difference of the vortex pair and, consequently, enhances mixing in the plug by increasing the folding effect.

If the viscosity ratio decreases further, the viscosity of plug 1 is much smaller than that of plug 2. The shear stress by plug 2

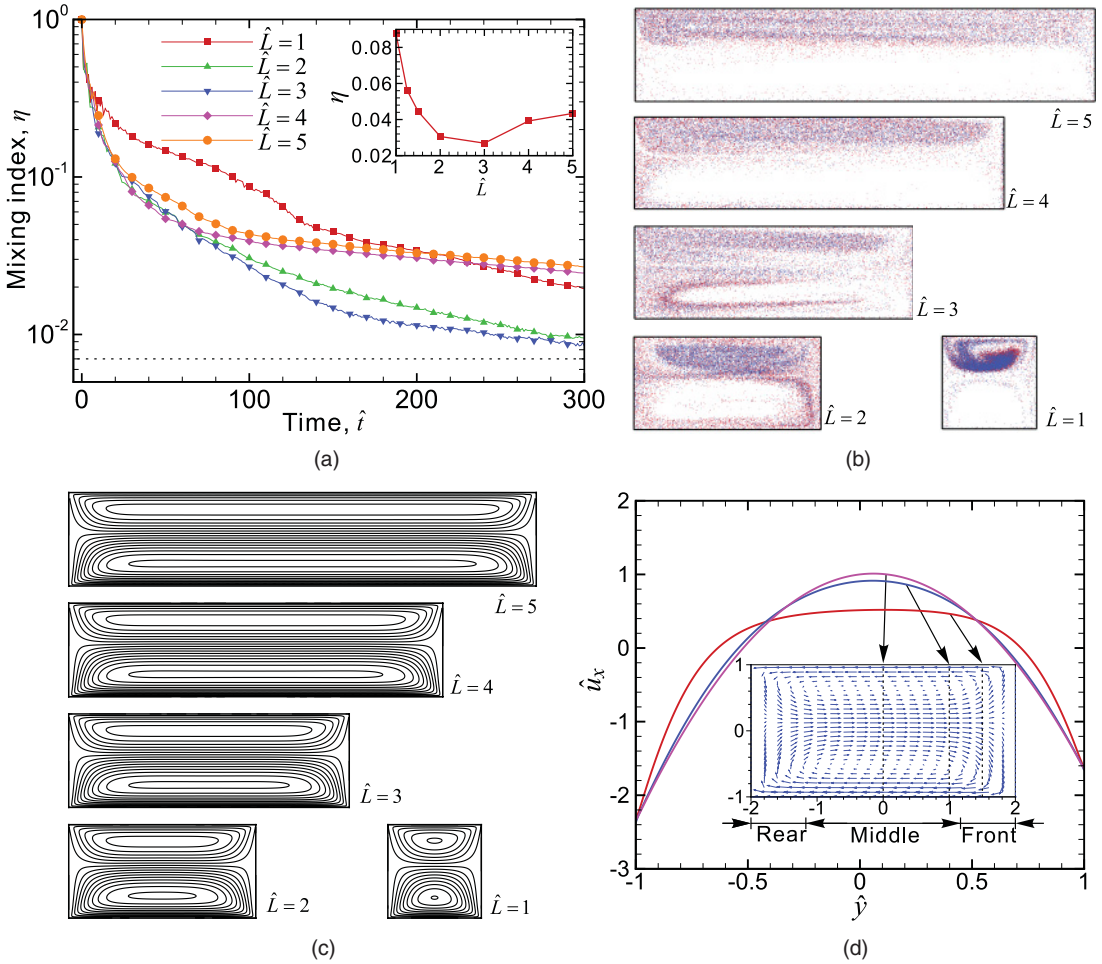

FIG. 10. (Color online) Effect of dimensionless plug length on mixing process in plugs. The radius ratio of the meandering microchannel is $\hat{R} = 0.7$, the Peclet number is $Pe = 10^4$, and the viscosity ratio is $\mu_1/\mu_2 = 1$. (a) Variation of mixing indices with time in plugs with different $\hat{L}$. The dashed horizontal line $\eta_{\text{asymp}} = 0.00707$ indicates the homogeneous state with randomly distributed particles. Inset: The variation of mixing indices with $\hat{L}$ at $\hat{t} = 100$. (b) Visualization of mixing patterns at $\hat{t} = 100$ for plugs with different $\hat{L}$. (c) Flow pattern in plugs of different $\hat{L}$. (d) The flow in a plug can be divided into three regions, the front region, the middle region, and the rear region. The velocity profiles at three typical cross sections, $\hat{x} = 0$, $\hat{x} = 1$, and $\hat{x} = 1.5$, are plotted. In the middle region (such as $\hat{x} = 0$), the velocity profile is parabolic, while in the front/rear regions (such as $\hat{x} = 1.5$), the velocity profile is flat in a large part of the transverse direction ($-0.5 < \hat{y} < 0.5$).

at the interface $\tau_{xy,2}$ is more significant, which not only affects the region near vortex **A**, but also affects the region near vortex **B**. If the shear stress $\tau_{xy,2}$, which is in the opposite direction from vortex **B**, is sufficiently strong, a secondary vortex is formed between the interface and vortex **B**, as illustrated in Fig. 9(b). The secondary vortices hinder the mixing in the plug because the transfer of species between vortices is limited by diffusion. The strength of the secondary vortices increases with the decrease in the viscosity ratio μ_1/μ_2. This phenomenon was observed numerically and experimentally by Sarrazin *et al.* [55,56] and by Blanchette [43]. They found that mixing is slow at the front and the rear of the droplets.

E. Effect of plug length

The effect of the plug length on the mixing process is shown in Fig. 10. The Peclet number and the viscosity ratio are fixed at $\text{Pe} = 10^4$ and $\mu_1/\mu_2 = 1$, respectively, while the dimensionless plug length $\hat{L}$ is varied from 1 to 5. The mixing indices are plotted against time for different $\hat{L}$ in Fig. 10(a). For long plugs, such as $\hat{L} = 5$, mixing is slow with a relatively high mixing index η. The mixing index decreases with decreasing $\hat{L}$, which indicates better mixing. If $\hat{L}$ decreases further, the mixing index η increases, which indicates that mixing becomes slow again. This effect can also be seen from the mixing patterns at $\hat{t} = 100$ for different $\hat{L}$ values, as shown in Fig. 10(b).

The effect of L on the mixing process is mainly due to its effect on flow patterns in plugs, as shown in Fig. 10(c). The flow in a plug can be divided into three regions—the front region, the middle region, and the rear region—as shown in the inset in Fig. 10(d). The front region and the rear region are dominated by transverse flow due to the presence of the front/rear interfaces, whereas the middle region is characterized by parallel flow without a significant interface effect. The length of the middle region increases with increasing $\hat{L}$. For long plugs ($\hat{L} = 5$), the middle region is long, therefore, a longer time is required for the particles to be advected for one cycle, and the parallel flows lead to slow mixing in the plug.

For short plugs, the middle region is short and most of the plug is affected by the transverse flow near the front/rear interfaces. The velocity profiles at three typical cross sections are plotted in Fig. 10(d). In the middle region, the velocity profile is parabolic, while in the front/rear regions, the velocity profile is flat in a large part of the transverse direction [$-0.5 < \hat{y} < 0.5$ as shown in Fig. 10(d)]. When flowing through the middle regions, liquid elements are stretched due to the velocity gradient. In contrast, when flowing through the front/rear region, liquid elements deform only slightly due to the flat velocity profile. Therefore, in short plugs, a blob of tracer particles may simply rotate under the recirculating flow but cannot be stretched into a long thin filament. Consequently, the mixing is relatively slow in short plugs, and plugs with a moderate $\hat{L}$ value are preferable for rapid mixing in meandering microchannels.

V. CONCLUSIONS

In this paper, a simplified two-dimensional model is proposed to investigate plug trains moving in meandering microchannels. The model is used to study the mixing process in plugs moving in meandering microchannels using the particle tracking method. The mixing process in plugs is the combined effect of the stretching of fluid filaments by the vortices, folding of fluid filaments by changing the direction of the channel curvature, and the diffusion of species between liquid filaments. The effects of the channel curvature, the Peclet number, the viscosity ratio, and the plug length are investigated. The results show that a large curvature, a low Peclet number, a moderate viscosity ratio, and a moderate plug length are preferred for good mixing in the plugs. The current study can help to optimize the micromixing in liquid plugs traveling in meandering microchannels and guide the design of lab-on-a-chip devices for applications such as chemical reactions, particle synthesis, and protein crystallization.

APPENDIX A: SOLUTION OF THE FLOW FIELD IN PLUG TRAINS

1. Boundary conditions of the liquid plugs

The stream function φ_i is constant at the boundary of plug i ($1 \leqslant i \leqslant N$), and it is set to be 0.

$$\varphi_i(x_i, -h) = 0, \quad \varphi_i(x_i, h) = 0, \tag{A1}$$

$$\varphi_i(-L_i, y_i) = 0, \quad \varphi_i(L_i, y_i) = 0. \tag{A2}$$

The sliding velocities at the walls are $-S_1$ and $-S_2$, respectively:

$$\frac{\partial}{\partial y_i}\varphi_i(x_i, h) = -S_1(t), \tag{A3}$$

$$\frac{\partial}{\partial y_i}\varphi_i(x_i, -h) = -S_2(t). \tag{A4}$$

At the interface of the two successive plugs, the velocity component u_x is:

$$\frac{\partial}{\partial y_i}\varphi_i(L_i, y_i) = 0, \quad \frac{\partial}{\partial y_i}\varphi_i(-L_i, y_i) = 0. \tag{A5}$$

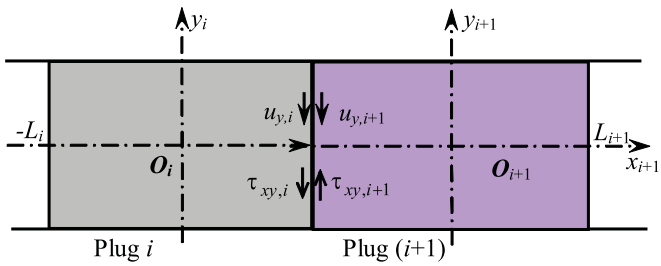

FIG. 11. (Color online) Matching of the velocity components (u_y) and the shear stresses (τ_{xy}) at the interface of two consecutive plugs [plug i and plug (i+1), where $1 \leqslant i < N$].

The tangential velocity component u_y and the shear stress τ_{xy} along the interface of the two consecutive plugs should be continuous across the interface, as illustrated in Fig. 11. From the velocities and the shear stresses at the right side of plug i and at the left side of plug (i+1), we have, respectively,

$$-\frac{\partial}{\partial x_i}\varphi_i(L_i, y_i) = -\frac{\partial}{\partial x_{i+1}}\varphi_{i+1}(-L_{i+1}, y_{i+1}), \tag{A6}$$

$$-\mu_i\frac{\partial^2}{\partial x_i^2}\varphi_i(L_i, y_i) = -\mu_{i+1}\frac{\partial^2}{\partial x_{i+1}^2}\varphi_{i+1}(-L_{i+1}, y_{i+1}), \tag{A7}$$

where $1 \leqslant i < N$. At the interface between plug 1 and plug N, the matching of the velocity components u_y and the shear stresses τ_{xy} applies between the right side of plug N and the left side of plug 1:

$$-\frac{\partial}{\partial x_N}\varphi_N(L_N, y_N) = -\frac{\partial}{\partial x_1}\varphi_1(-L_1, y_1), \tag{A8}$$

$$-\mu_N\frac{\partial^2}{\partial x_N^2}\varphi_N(L_N, y_N) = -\mu_1\frac{\partial^2}{\partial x_1^2}\varphi_1(-L_1, y_1), \tag{A9}$$

2. Nondimensionalization

Using half of the channel width h as the characteristic length and plug velocity V as the characteristic velocity to nondimensionalize the governing equation (3) and the boundary conditions [Eqs. (A1) through (A9)], we have, for plug i ($1 \leqslant i \leqslant N$),

$$\begin{aligned} &\hat{x}_i \equiv x_i/h, \quad \hat{y}_i \equiv y_i/h, \quad \hat{L}_i \equiv L_i/h, \\ &\hat{u}_{x,i} \equiv u_{x,i}/V, \quad \hat{u}_{y,i} \equiv u_{y,i}/V, \quad \hat{\varphi}_i \equiv \varphi_i/(hV), \end{aligned} \tag{A10}$$

where $\hat{L}_i$ is the dimensionless plug length of plug i. The dimensionless governing equation is

$$\left(\frac{\partial^4}{\partial \hat{x}_i^4} + 2\frac{\partial^4}{\partial \hat{x}_i^2 \partial \hat{y}_i^2} + \frac{\partial^4}{\partial \hat{y}_i^4}\right)\hat{\varphi}_i = 0. \tag{A11}$$

The boundary conditions are

$$\hat{\varphi}_i(\hat{x}_i, -1) = 0, \quad \hat{\varphi}_i(\hat{x}_i, 1) = 0, \tag{A12}$$

$$\hat{\varphi}_i(-\hat{L}_i, \hat{y}_i) = 0, \quad \hat{\varphi}_i(\hat{L}_i, \hat{y}_i) = 0, \tag{A13}$$

$$\frac{\partial}{\partial \hat{y}_i}\hat{\varphi}_i(\hat{x}_i, 1) = -\xi_1(\hat{t}), \quad \frac{\partial}{\partial \hat{y}_i}\hat{\varphi}_i(\hat{x}_i, -1) = -\xi_2(\hat{t}), \tag{A14}$$

$$\frac{\partial}{\partial \hat{y}_i}\hat{\varphi}_i(\hat{L}_i, \hat{y}_i) = 0, \quad \frac{\partial}{\partial \hat{y}_i}\hat{\varphi}_i(-\hat{L}_i, \hat{y}_i) = 0, \tag{A15}$$

where $1 \leqslant i < N$, $\xi_1(\hat{t}) \equiv S_1(t)/V$, and $\xi_2(\hat{t}) \equiv S_2(t)/V$. The matching of velocity components and shear stresses at the interface of two consecutive plugs yields

$$\frac{\partial}{\partial \hat{x}_i}\hat{\varphi}_i(\hat{L}_i,\hat{y}_i) = \frac{\partial}{\partial \hat{x}_{i+1}}\hat{\varphi}_{i+1}(-\hat{L}_{i+1},\hat{y}_{i+1}), \tag{A16}$$

$$\hat{\mu}_i \frac{\partial^2}{\partial \hat{x}_i^2}\hat{\varphi}_i(\hat{L}_i,\hat{y}_i) = \hat{\mu}_{i+1}\frac{\partial^2}{\partial \hat{x}_{i+1}^2}\hat{\varphi}_{i+1}(-\hat{L}_{i+1},\hat{y}_{i+1}), \tag{A17}$$

$$\frac{\partial}{\partial \hat{x}_N}\hat{\varphi}_N(\hat{L}_N,\hat{y}_N) = \frac{\partial}{\partial \hat{x}_1}\hat{\varphi}_1(-\hat{L}_1,\hat{y}_1), \tag{A18}$$

$$\hat{\mu}_N \frac{\partial^2}{\partial \hat{x}_N^2}\hat{\varphi}_N(\hat{L}_N,\hat{y}_N) = \hat{\mu}_1\frac{\partial^2}{\partial \hat{x}_1^2}\hat{\varphi}_1(-\hat{L}_1,\hat{y}_1), \tag{A19}$$

where $\hat{\mu}_i \equiv \mu_i/\mu_0$ is the viscosity ratio, with μ_0 as a reference viscosity.

3. Series solution

The format of the solution of the biharmonic equation for plug i can be constructed as [57]

$$\hat{\varphi}_i(\hat{x}_i,\hat{y}_i) = \sum_{m=1}^{\infty}\frac{(-1)^m}{\alpha_m}\left[p_m^o(\hat{y}_i)X_m^o + p_m^e(\hat{y}_i)X_m^e\right]\cos(\alpha_m\hat{x}_i) + \hat{L}_i\sum_{l=1}^{\infty}\frac{(-1)^l}{\beta_l}\left[q_l^e(\hat{x}_i)Y_l^e + q_l^o(\hat{x}_i)Y_l^o\right]\sin(\beta_l\hat{y}_i), \tag{A20}$$

where

$$\alpha_m = \frac{2m-1}{2\hat{L}_i}\pi, \tag{A21}$$

$$\beta_l = l\pi, \tag{A22}$$

$$p_m^o(\hat{y}_i) = \frac{\sinh(\alpha_m\hat{y}_i)}{\cosh(\alpha_m)} - \hat{y}_i\tanh(\alpha_m)\frac{\cosh(\alpha_m\hat{y}_i)}{\cosh(\alpha_m)}, \tag{A23}$$

$$p_m^e(\hat{y}_i) = \tanh(\alpha_m)\frac{\cosh(\alpha_m\hat{y}_i)}{\cosh(\alpha_m)} - \hat{y}_i\frac{\sinh(\alpha_m\hat{y}_i)}{\cosh(\alpha_m)}, \tag{A24}$$

$$q_l^o(\hat{x}_i) = \hat{L}_i\frac{\sinh(\beta_l\hat{x}_i)}{\cosh(\beta_l\hat{L}_i)} - \hat{x}_i\tanh(\beta_l\hat{L}_i)\frac{\cosh(\beta_l\hat{x}_i)}{\cosh(\beta_l\hat{L}_i)}, \tag{A25}$$

$$q_l^e(\hat{x}_i) = \hat{L}_i\tanh(\beta_l\hat{L}_i)\frac{\cosh(\beta_l\hat{x}_i)}{\cosh(\beta_l\hat{L}_i)} - \hat{x}_i\frac{\sinh(\beta_l\hat{x}_i)}{\cosh(\beta_l\hat{L}_i)}. \tag{A26}$$

The values of Eqs. (A23) through (A26) are all 0 at the end points of the intervals $-\hat{L}_i \leqslant \hat{x}_i \leqslant -\hat{L}_i$ and $-1 \leqslant \hat{y}_i \leqslant 1$. This setting can make Eqs. (A23) through (A26) satisfy the biharmonic equation and the homogeneous boundary conditions of $\hat{\varphi}_i = 0$ at the boundary. The coefficients X_m^o, X_m^e, Y_l^o, and Y_l^e of $\hat{\varphi}_i(\hat{x}_i,\hat{y}_i)$ in Eq. (A20) can be obtained from boundary conditions of velocity [Eqs. (A14), (A16), and (A18)] and shear stress [Eqs. (A17) and (A19)].

From the dimensionless stream function in Eq. (A20), the dimensionless velocity field can be obtained as

$$\hat{u}_{x,i} \equiv \frac{\partial}{\partial \hat{y}_i}\hat{\varphi}_i(\hat{x}_i,\hat{y}_i) = \sum_{m=1}^{\infty}\left[p_m^{o\prime}(\hat{y}_i)X_m^o + p_m^{e\prime}(\hat{y}_i)X_m^e\right]\frac{(-1)^m}{\alpha_m}\cos(\alpha_m\hat{x}_i) + \hat{L}_i\sum_{l=1}^{\infty}(-1)^l\left[q_l^e(\hat{x}_i)Y_l^e + q_l^o(\hat{x}_i)Y_l^o\right]\cos(\beta_l\hat{y}_i), \tag{A27}$$

$$\hat{u}_{y,i} \equiv -\frac{\partial}{\partial \hat{x}_i}\varphi(\hat{x}_i,\hat{y}_i) = \sum_{m=1}^{\infty}\left[p_m^o(\hat{y}_i)X_m^o + p_m^e(\hat{y}_i)X_m^e\right](-1)^m\sin(\alpha_m\hat{x}_i) - \hat{L}_i\sum_{l=1}^{\infty}\frac{(-1)^l}{\beta_l}\left[q_l^{e\prime}(\hat{x}_i)Y_l^e + q_l^{o\prime}(\hat{x}_i)Y_l^o\right]\sin(\beta_l\hat{y}_i), \tag{A28}$$

where

$$p_m^{o\prime}(\hat{y}_i) = [\alpha_m - \tanh(\alpha_m)]\frac{\cosh(\alpha_m\hat{y}_i)}{\cosh(\alpha_m)} - \hat{y}_i\alpha_m\tanh(\alpha_m)\frac{\sinh(\alpha_m\hat{y}_i)}{\cosh(\alpha_m)}, \tag{A29}$$

$$p_m^{e\prime}(\hat{y}_i) = [\alpha_m\tanh(\alpha_m) - 1]\frac{\sinh(\alpha_m\hat{y}_i)}{\cosh(\alpha_m)} - \hat{y}_i\alpha_m\frac{\cosh(\alpha_m\hat{y}_i)}{\cosh(\alpha_m)}, \tag{A30}$$

$$q_l^{o\prime}(\hat{x}_i) = [\beta_l\hat{L}_i - \tanh(\beta_l\hat{L}_i)]\frac{\cosh(\beta_l\hat{x}_i)}{\cosh(\beta_l\hat{L}_i)} - \hat{x}_i\beta_l\tanh(\beta_l\hat{L}_i)\frac{\sinh(\beta_l\hat{x}_i)}{\cosh(\beta_l\hat{L}_i)}, \tag{A31}$$

$$q_l^{e\prime}(\hat{x}_i) = [\beta_l\hat{L}_i\tanh(\beta_l\hat{L}_i) - 1]\frac{\sinh(\beta_l\hat{x}_i)}{\cosh(\beta_l\hat{L}_i)} - \hat{x}_i\beta_l\frac{\cosh(\beta_l\hat{x}_i)}{\cosh(\beta_l\hat{L}_i)}. \tag{A32}$$

Introducing a modified Fourier transform FX [57],

$$\mathrm{FX}[f(\hat{x}_i)] \equiv \frac{(-1)^{m-1}}{\hat{L}_i}\int_{-\hat{L}_i}^{\hat{L}_i} f(\hat{x}_i)\cos(\alpha_m\hat{x}_i)\,d\hat{x}_i. \tag{A33}$$

Applying the modified Fourier transform FX to Eq. (A14) yields

$$\frac{4\xi_1(\hat{t})\alpha_m}{\pi\,(2m-1)} = -\left[\Delta_1^o\,(\alpha_m)\,X_m^o + \Delta_1^e\,(\alpha_m)\,X_m^e\right] + \sum_{l=1}^{\infty}\frac{4\alpha_m^2\beta_l Y_l^e}{\left(\alpha_m^2+\beta_l^2\right)^2}, \tag{A34}$$

$$\frac{4\xi_2\left(\hat{t}\right)\alpha_m}{\pi\,(2m-1)} = -\left[\Delta_1^o\,(\alpha_m)\,X_m^o - \Delta_1^e\,(\alpha_m)\,X_m^e\right] + \sum_{l=1}^{\infty}\frac{4\alpha_m^2\beta_l Y_l^e}{\left(\alpha_m^2+\beta_l^2\right)^2}, \tag{A35}$$

where

$$\Delta_1^o\,(\alpha_m) \equiv p_m^{o\,\prime}\,(\hat{y}_i=1) = \frac{\alpha_m}{\cosh^2(\alpha_m)} - \tanh(\alpha_m), \tag{A36}$$

$$\Delta_1^e\,(\alpha_m) \equiv p_m^{e\,\prime}\,(\hat{y}_i=1) = \frac{-\alpha_m}{\cosh^2(\alpha_m)} - \tanh(\alpha_m). \tag{A37}$$

Introducing another modified Fourier transform FY,

$$\mathrm{FY}[f\,(\hat{y}_i)] \equiv (-1)^{l-1}\int_{-1}^{1} f\,(\hat{y}_i)\sin(\beta_l\hat{y}_i)\,d\hat{y}_i. \tag{A38}$$

Applying the modified Fourier transform FY to Eqs. (A16) and (A17) yields

$$\left[-\sum_{m=1}^{\infty}X_m^o\frac{4\alpha_m\beta_l^2\tanh^2(\alpha_m)}{\left(\alpha_m^2+\beta_l^2\right)^2} + \hat{L}\left[\Delta_2^e(\beta_l\hat{L})Y_l^e + \Delta_2^o(\beta_l\hat{L})Y_l^o\right]\right]_{\text{Plug } i}$$

$$= \left[\sum_{m=1}^{\infty}X_m^o\frac{4\alpha_m\beta_l^2\tanh^2(\alpha_m)}{\left(\alpha_m^2+\beta_l^2\right)^2} + \hat{L}\left[-\Delta_2^e(\beta_l\hat{L})Y_l^e + \Delta_2^o(\beta_l\hat{L})Y_l^o\right]\right]_{\text{Plug } (i+1)}, \tag{A39}$$

$$\left[\mu\left[\Delta_3^e(\beta_l\hat{L})Y_l^e + \Delta_3^o(\beta_l\hat{L})Y_l^o\right]\right]_{\text{Plug } i} = \left[\mu\left[\Delta_3^e(\beta_l\hat{L})Y_l^e - \Delta_3^o(\beta_l\hat{L})Y_l^o\right]\right]_{\text{Plug } (i+1)}, \tag{A40}$$

where

$$\Delta_2^o(\beta_l\hat{L}_i) \equiv \beta_l\hat{L}_i - \tanh(\beta_l\hat{L}_i) - (\beta_l\hat{L}_i)\tanh^2(\beta_l\hat{L}_i), \tag{A41}$$

$$\Delta_2^e(\beta_l\hat{L}_i) \equiv -\beta_l\hat{L}_i - \tanh(\beta_l\hat{L}_i) + (\beta_l\hat{L}_i)\tanh^2(\beta_l\hat{L}_i), \tag{A42}$$

$$\Delta_3^o(\beta_l\hat{L}_i) \equiv 2\beta_l\hat{L}_i\tanh^2(\beta_l\hat{L}_i), \tag{A43}$$

$$\Delta_3^e(\beta_l\hat{L}_i) \equiv -2\beta_l\hat{L}_i. \tag{A44}$$

Similarly, applying the modified Fourier transform FY to Eqs. (A18) and (A19) yields, respectively,

$$\left[-\sum_{m=1}^{\infty}X_m\frac{4\alpha_m\beta_l^2\tanh^2(\alpha_m)}{\left(\alpha_m^2+\beta_l^2\right)^2} + \hat{L}\left[\Delta_2^e(\beta_l\hat{L}_i)Y_l^e + \Delta_2^o(\beta_l\hat{L})Y_l^o\right]\right]_{\text{Plug } N}$$

$$= \left[\sum_{m=1}^{\infty}X_m\frac{4\alpha_m\beta_l^2\tanh^2(\alpha_m)}{\left(\alpha_m^2+\beta_l^2\right)^2} + \hat{L}\left[-\Delta_2^e(\beta_l\hat{L}_i)Y_l^e + \Delta_2^o(\beta_l\hat{L})Y_l^o\right]\right]_{\text{Plug1}}, \tag{A45}$$

$$\left[\mu\left[\Delta_3^e(\beta_l\hat{L})Y_l^e + \Delta_3^o(\beta_l\hat{L})Y_l^o\right]\right]_{\text{Plug } N} = \left[\mu\left[\Delta_3^e(\beta_l\hat{L})Y_l^e - \Delta_3^o(\beta_l\hat{L})Y_l^o\right]\right]_{\text{Plug1}}. \tag{A46}$$

Equations (A34), (A35), (A39), (A40), (A45), and (A46) form a set of infinite algebra linear equations like $AX = b$, with unknowns X_m^e, X_m^o, Y_l^e, and Y_l^o. The number of unknowns is $4N \times \infty$, and the number of equations is $4N \times \infty$, where ∞ corresponds to the coefficients of the infinite series. These equations can be solved using the method of reduction [57,58] by truncating the infinite series after the first N^* terms. Therefore, the number of unknowns reduces to $4N \times N^*$,

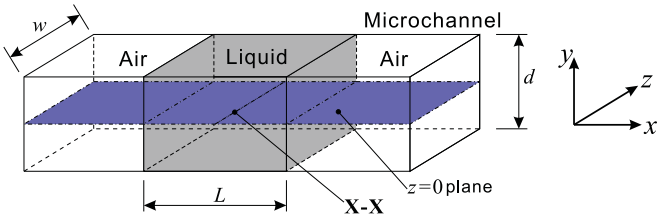

FIG. 12. (Color online) Schematic diagram of a 3D liquid plug moving in a 3D microchannel. The width of the microchannel is w. The depth of the microchannel is d. The plug length is L. The middle depth plane $z = 0$ is indicated.

and the solution precision can be as high as needed by increasing N^*.

APPENDIX B: EFFECT OF CHANNEL DEPTH ON FLOW PATTERN WITHIN PLUG FLOW

To examine the 2D assumption, and to study the 3D effect on the flow pattern within liquid plugs, numerical simulations were carried out using Fluent (version 13.0; Ansys Inc.) with the finite volume method (FVM). The dimension of the microchannel is shown in Fig. 12. Grid independence was tested by repeating refinement of the grid until grid-independent solutions were obtained. The number of control volumes for each plug was around 10^5.

The numerical results are shown in Fig. 13. For a small d, the flow pattern in the liquid plug is affected by the top and bottom walls of the microchannel. As the depth of the microchannel increases, the effect of the top and the bottom walls decreases, and the flow profile along **X-X** gradually approaches an unchanged shape. Figure 13(c) shows that the flow in the middle cross section $z = 0$ can be regarded as 2D when the depth of the channel is $d > 5w$. Therefore, for microchannels with depths of $d > 5w$, the 2D model can accurately predict the flow in the liquid plug. For microchannels with depths $d < 5w$, the accuracy of the 2D model is reduced, but it can still qualitatively predict the two counter-rotating vortices, which is a significant feature of plug flow.

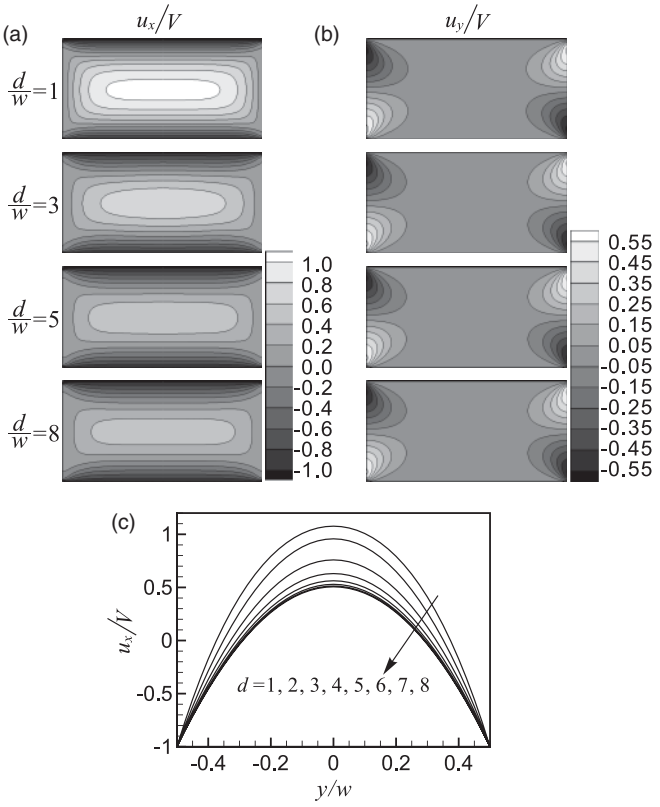

FIG. 13. Effect of the channel depth on the flow pattern in plugs. The width of the microchannel is w, the depth of the channel d is varied from w to $8w$, and the length of the plug is $L = 2w$. The Reynolds number $\mathrm{Re} = \frac{\rho V w}{\mu} = 10^{-2}$. (a) Contours of velocity component u_x/V in the middle depth plane $z = 0$ as indicated in Fig. 12. (b) Contours of velocity component u_y/V in the middle depth plane $z = 0$. (c) Profiles of u_x/V along **X-X** indicated in Fig. 12.

[1] H. Song, D. L. Chen, and R. F. Ismagilov, Angew. Chem., Int. Ed. Engl. **45**, 7336 (2006).
[2] D. Dendukuri and P. S. Doyle, Adv. Mater. **21**, 4071 (2009).
[3] L. Li and R. F. Ismagilov, Annu. Rev. Biophys. **39**, 139 (2010).
[4] S.-W. Choi, Y. Zhang, and Y. Xia, Angew. Chem., Int. Ed. Engl. **49**, 7904 (2010).
[5] L. Y. Yeo, H. C. Chang, P. P. Y. Chan, and J. R. Friend, Small **7**, 12 (2011).
[6] N. T. Nguyen and Z. Wu, J. Micromech. Microeng. **15**, R1 (2005).
[7] N.-T. Nguyen, *Micromixers: Fundamentals, Design and Fabrication*, *Micro & Nano Technologies* (William Andrew, Norwich, NY, 2008).
[8] T. M. Squires and S. R. Quake, Rev. Mod. Phys. **77**, 977 (2005).
[9] W. Y. Ng, S. Goh, Y. C. Lam, C. Yang, and I. Rodíguez, Lab Chip **9**, 802 (2009).
[10] S. H. Lee, D. van Noort, J. Y. Lee, B.-T. Zhang, and T. H. Park, Lab Chip **9**, 479 (2009).
[11] D. Ahmed, X. Mao, B. K. Juluri, and T. J. Huang, Microfluid. Nanofluid. **7**, 727 (2009).
[12] D. L. Vainchtein, J. Widloski, and R. O. Grigoriev, Phys. Fluids **19**, 067102 (2007).
[13] N.-T. Nguyen and X. Huang, Lab Chip **5**, 1320 (2005).
[14] F. G. Bessoth, A. J. DeMello, and A. Manz, Anal. Commun. **36**, 213 (1999).
[15] V. Hessel, S. Hardt, H. Löwe, and F. Schönfeld, AIChE J. **49**, 566 (2003).
[16] R. Miyake, T. S. J. Lammerink, M. Elwenspoek, and J. H. J. Fluitman, in *Proceedings of the 1993 IEEE Micro Electro Mechanical Systems—MEMS* (Fort Lauderdale, 1993), pp. 248–253.
[17] J. B. Knight, A. Vishwanath, J. P. Brody, and R. H. Austin, Phys. Rev. Lett. **80**, 3863 (1998).

[18] J. R. Burns and C. Ramshaw, Lab Chip **1**, 10 (2001).
[19] K. Handique and M. A. Burns, J. Micromech. Microeng. **11**, 548 (2001).
[20] M. Rhee and M. A. Burns, Langmuir **24**, 590 (2007).
[21] S. Y. Teh, R. Lin, L. H. Hung, and A. P. Lee, Lab Chip **8**, 198 (2008).
[22] J. D. Tice, H. Song, A. D. Lyon, and R. F. Ismagilov, Langmuir **19**, 9127 (2003).
[23] H. Aref, J. Fluid. Mech. **143**, 1 (1984).
[24] J. M. Ottino, *The Kinematics of Mixing: Stretching, Chaos, and Transport* (Cambridge University Press, Cambridge, 1989).
[25] A. D. Stroock, S. K. W. Dertinger, A. Ajdari, I. Mezic, H. A. Stone, and G. M. Whitesides, Science **295**, 647 (2002).
[26] X. Niu and Y. K. Lee, J. Micromech. Microeng. **13**, 454 (2003).
[27] S. Qian and H. H. Bau, Anal. Chem. **74**, 3616 (2002).
[28] A. D. Stroock and G. M. Whitesides, Acc. Chem. Res. **36**, 597 (2003).
[29] D. W. Oh, J. S. Jin, J. H. Choi, H. Y. Kim, and J. S. Lee, J. Micromech. Microeng. **17**, 2077 (2007).
[30] H. Song, J. D. Tice, and R. F. Ismagilov, Angew. Chem., Int. Ed. Engl. **42**, 768 (2003).
[31] F. Trachsel, A. Günther, S. Khan, and K. F. Jensen, Chem. Eng. Sci. **60**, 5729 (2005).
[32] H. Song, M. R. Bringer, J. D. Tice, C. J. Gerdts, and R. F. Ismagilov, Appl. Phys. Lett. **83**, 4664 (2003).
[33] K.-Y. Tung, C.-C. Li, and J.-T. Yang, Microfluid. Nanofluid. **7**, 545 (2009).
[34] D. M. Fries and P. R. von Rohr, Chem. Eng. Sci. **64**, 1326 (2009).
[35] N. Harries, J. R. Burns, D. A. Barrow, and C. Ramshaw, Int. J. Heat Mass Transf. **46**, 3313 (2003).
[36] M. N. Kashid, I. Gerlach, S. Goetz, J. Franzke, J. F. Acker, F. Platte, D. W. Agar, and S. Turek, Ind. Eng. Chem. Res. **44**, 5003 (2005).
[37] M. Muradoglu, A. Günther, and H. A. Stone, Phys. Fluids **19**, 072109 (2007).
[38] H. Dogan, S. Nas, and M. Muradoglu, Int. J. Multiphase Flow **35**, 1149 (2009).
[39] M. Muradoglu and H. A. Stone, Phys. Fluids **17**, 1 (2005).
[40] H. K. Versteeg and W. Malalasekera, *An Introduction to Computational Fluid Dynamics: The Finite Volume Method*, 2nd ed. (Pearson Education, New York, 2007).
[41] C. C. Chang and R. J. Yang, J. Micromech. Microeng. **16**, 1453 (2006).
[42] T. G. Kang and T. H. Kwon, J. Micromech. Microeng. **14**, 891 (2004).
[43] F. Blanchette, Phys. Rev. E **80**, 066316 (2009).
[44] D. Kroujiline and H. A. Stone, Physica D **130**, 105 (1999).
[45] Z. B. Stone and H. A. Stone, Phys. Fluids **17**, 1 (2005).
[46] W. R. Dean, Proc. R. Soc. London A **121**, 402 (1928).
[47] Z. Che, T. N. Wong, and N. T. Nguyen, Int. J. Heat Mass Transf. **53**, 1977 (2010).
[48] J. Sivasamy, Z. Che, T. N. Wong, N.-T. Nguyen, and L. Yobas, Chem. Eng. Sci. **65**, 5382 (2010).
[49] J. Happel and H. Brenner, *Low Reynolds Number Hydrodynamics: With Special Applications to Particulate Media*, 2nd ed. (Martinus Nijhoff, The Hague, 1983).
[50] V. V. Meleshko, Appl. Mech. Rev. **56**, 33 (2003).
[51] P. N. Shankar, *Slow Viscous Flows: Qualitative Features and Quantitative Analysis Using Complex Eigenfunction Expansions* (Imperial College Press, London, 2007).
[52] A. Günther, M. Jhunjhunwala, M. Thalmann, M. A. Schmidt, and K. F. Jensen, Langmuir **21**, 1547 (2005).
[53] M. Funakoshi, Fluid. Dyn. Res. **40**, 1 (2008).
[54] J. H. Phelps and C. L. Tucker III, Chem. Eng. Sci. **61**, 6826 (2006).
[55] F. Sarrazin, K. Loubière, L. Prat, C. Gourdon, T. Bonometti, and J. Magnaudet, AIChE J. **52**, 4061 (2006).
[56] F. Sarrazin, T. Bonometti, L. Prat, C. Gourdon, and J. Magnaudet, Microfluid. Nanofluid. **5**, 131 (2008).
[57] V. V. Meleshko, Proc. R. Soc. London A **452**, 1999 (1996).
[58] Y. Song, J. Xu, and Y. Yang, Phys. Fluids **22**, 072003 (2010).